

# Effect of Rare Earth Ion Substitution on Phase Decomposition of Apatite Structure

Geeta Sharma,<sup>\*[a]</sup> Sarathkumar Loganathan,<sup>[a]</sup> Eric K. Barimah,<sup>[a]</sup> Paraskevi Georgopoulou,<sup>[a]</sup> Esther Taylor,<sup>[a]</sup> Andrew J. Scott,<sup>[a]</sup> Simon Strafford,<sup>[a]</sup> and Animesh Jha<sup>[a]</sup>

The paper describes an investigation of phase decomposition of apatite lattice doped with rare earth ions (cerium, samarium, and holmium) at temperatures ranging from 25–1200 °C. The rare-earth ion-doped apatite minerals were synthesized using the sol-gel method. *In situ* high-temperature powder X-ray diffraction (XRD) was used to observe the phase changes and the lattice parameters were analyzed to ascertain the crystallographic transformations. The expansion coefficient of the compounds was determined, and it was found that the *c*-axis was the most expandable due to relatively weak chemical bonds along the *c*-crystallographic axis. Differential scanning calorimetry (DSC) and thermogravimetric analysis (TGA) were used to examine the decomposition properties of the materials.

Due to rare earth ion doping, the produced materials had slightly variable decomposition behaviour. The cerium and samarium ions were present in multiple oxidation states (Ce<sup>3+</sup>, Ce<sup>4+</sup>, Sm<sup>3+</sup>, Sm<sup>2+</sup>), whereas only Ho<sup>3+</sup> ions were observed. Rare earth ion substitution affects tri-calcium phosphate proportion during decomposition by regulating concentrations of vacancies. X-ray photoelectron spectroscopy (XPS) analysis indicated that cerium and samarium ion-doped apatite yielded only 25% tricalcium phosphate during decomposition. This finding advances our understanding of apatite structures, with implications for various high-temperature processes like calcination, sintering, hydrothermal processing, and plasma spraying.

## 1. Introduction

The apatite supergroup encompasses minerals characterized by a generic chemical formula of  $^{IX}M_1Z^{VI}M_2Z^{IV}(TO_4)_3X$  (with  $Z=2$ ), where they can chemically manifest as phosphates, arsenates, vanadates, silicates, and sulphates. While the maximum space group symmetry is  $P6_3/m$ , numerous members of this supergroup exhibit lower symmetry levels due to cation ordering and deviations from the ideal topology. These deviations may lead to an increase in the number of independent sites within the structure. The diverse array of ions that can occupy pivotal sites [ $M=Ca^{2+}$ ,  $Pb^{2+}$ ,  $Ba^{2+}$ ,  $Sr^{2+}$ ,  $Mn^{2+}$ ,  $Na^+$ ,  $Ce^{3+}$ ,  $La^{3+}$ ,  $Y^{3+}$ ,  $Bi^{3+}$ ;  $T=P^{5+}$ ,  $As^{5+}$ ,  $V^{5+}$ ,  $Si^{4+}$ ,  $S^{6+}$ ,  $B^{3+}$ ;  $X=F$ , (OH), Cl] gives rise to a multitude of compositions, each potentially classified as distinct mineral species.<sup>[1,2]</sup> These minerals are categorized based on the detection of elevated concentrations of OH<sup>−</sup>, F<sup>−</sup>, Cl<sup>−</sup>, or Br<sup>−</sup> ions in the natural minerals. Apatite minerals are essential in the formation of various rocks such as metamorphic, igneous and sedimentary rocks, as well as in biological tissues such as bones and teeth. Because of the high concentrations of phosphorus, the mineral is a primary source for fertilizer

manufacturing, phosphoric acid, and for bone and dental tissue restorative materials.<sup>[2–4]</sup>

Apatite compounds exhibit a distinctive structural arrangement characterized by discrete phosphate tetrahedra (AO<sub>4</sub>) interconnected by the cation polyhedra, which collectively form layered structures.<sup>[5]</sup> Apatite-type structures have two cationic sites, namely 4f and 6h both having different local symmetry and coordination number.<sup>[5]</sup> The ratio of ions residing at these sites is 4f:6h = 2:3. The versatility of calcium-ion-based apatite stems from its distinctive capacity for ionic substitution, active surface characteristics, and the degree of crystallinity.<sup>[6,7]</sup> These characteristics give calcium apatite its multifunctional nature, enabling it to be used in a variety of applications, including drug delivery systems, bioceramics and coatings, bone regeneration and implants, diagnostic imaging (contrast agents for medical imaging techniques) and wastewater treatment etc.<sup>[8]</sup> Advancing our understanding of the intricate relationship between processing, microstructure, and property is crucial. The process dependent structure-property relationship is of paramount importance in determining the targeted applications of tailored apatite minerals. For instance, the production of apatite-based materials, which have uses in waste remediation, lighting, and biomaterials, requires high-temperature processing.<sup>[8–10]</sup>

The Ca/P ratio, structural substitution and the gas composition affects the phase stability of apatite structure while heating.<sup>[11–15]</sup> Notably, the substitution of calcium and phosphate significantly decrease thermal stability, leading to phase instability at temperatures below 900 °C. The anions in the hexagonal axis, OH in HAp, F in FAp and Cl in ClAp are the last to leave upon heating, and prevention of the loss of these groups ensures high temperature stability.<sup>[16]</sup> The stability of

[a] G. Sharma, S. Loganathan, E. K. Barimah, P. Georgopoulou, E. Taylor, A. J. Scott, S. Strafford, A. Jha  
Faculty of Engineering and Physical Sciences, School of Chemical and Process Engineering, University of Leeds, Leeds LS2 9JT, United Kingdom  
E-mail: g.sharma@leeds.ac.uk

Supporting information for this article is available on the WWW under <https://doi.org/10.1002/cphc.202400109>

© 2024 The Authors. ChemPhysChem published by Wiley-VCH GmbH. This is an open access article under the terms of the Creative Commons Attribution License, which permits use, distribution and reproduction in any medium, provided the original work is properly cited.

apatite is determined by the anion position in the hexagonal axis and decreases in the following order  $F > Cl > OH$ .

The current work examines the phase transformation properties of apatites containing rare-earth ions ( $Ce^{3+}$ ,  $Sm^{3+}$ , and  $Ho^{3+}$ ) over a wide temperature range (25–1200 °C). The inclusion of rare earth ions, namely  $Ce^{3+}$ ,  $Sm^{3+}$ , and  $Ho^{3+}$ , in the study serves to examine their synergistic effects on phase transformation within the apatite lattice. These ions were chosen based on their varying size and electronegativity to understand the influence on phase stability of apatites. The dilute solid solutions of rare earth and  $F^-$  ions are investigated with reference to their phase stability when such apatite minerals are in equilibrium with aqueous phase media (pH 5.5–7.1 in human body).<sup>[17]</sup> The impact of rare earth ion substitution on the thermal expansion and phase transitions and decomposition of apatites has been investigated using the high temperature *in situ* X-ray diffraction. Using thermogravimetric analysis (TGA) we analysed the effect of temperature and multivalent-RE-ion induced dimensional changes in apatite minerals. The changes in the structure of apatites after heat treatment were investigated by high-resolution X-ray photoelectron spectroscopy (XPS) and Fourier transform infrared spectroscopy (FTIR) analysis. There are reports available regarding the investigations on the thermal stability of apatite structures with a wide range of substitutions such as transition metal ions, halogens etc.<sup>[16]</sup> However, the investigations pertaining to the effect of rare-earth ions on phase stability are limited. The present investigation aims to improve our understanding on phase decomposition mechanism that is influenced by the substitution of  $Ca^{2+}$  ions with selected rare earth ions and in the presence of fluoride ion. The analysis of phase decomposition is relevant in controlling the structure and properties of bioceramic during manufacturing, thermal barrier coatings, refractory materials, gas sensing at elevated temperatures and molten salt reactors.

## Experimental Section

### Synthesis of Apatites

The rare earth-doped hydroxyapatite (strontium doped (2 mole%) OH-bearing fluorapatite) was synthesized by the sol-gel process.<sup>[17]</sup> The host matrix was doped with 2 mole% of Ce in place of Ca, and 2 mole% of phosphate was replaced with fluorine. Further to study the effect of increased concentration of doping on the structural properties, the prepared apatites were double, and triple-doped

with other rare earth ions ( $Sm^{3+}$ ,  $Ho^{3+}$ ). The various compositions synthesized are listed in Table 1. In a typical synthesis procedure, calculated quantities of calcium nitrate, strontium nitrate, and cerium nitrate were dissolved in 1000 ml of distilled water (solution A) followed by heating to 45 °C. In a separate beaker, an aqueous solution of ammonium fluoride and ammonium phosphate were prepared in 1000 ml (solution B) by adding their calculated amounts. After stabilising the temperature of solution, A to 45 °C, solution B was added dropwise to it while maintaining the basic pH (9–10) of the solution. The final solution was stirred for 1 h at 45 °C. During the whole synthesis procedure, the top of the beaker was sealed to prevent the ingress of  $CO_2$  into the mineral solution. The precipitates formed were allowed to age for 24 h at room temperature. The precipitates obtained were filtered using filter paper (Whatman grade 44 with pores of 3  $\mu m$ ), washed several times with distilled water, and then freeze-dried.

### Experimental Techniques

The high temperature phase transitions were examined by using *in situ* X-ray diffraction analysis. The experiments were performed in a high temperature chamber Anton Paar HTK 1200 N placed on a powder diffractometer Panalytical X'Pert Pro, with a temperature range of 25 [room temperature (RT)] °C to 1200 °C. The scans were recorded from 20° to 70° with a scan step of 0.013°.

Using the fluorapatite,  $OH^-$ ,  $F^-$  bearing crystal structure (04-015-6661), Rietveld refinement of the powder X-ray diffraction (PXRD) data was performed from 20°–70° using high-score software. The Bragg reflections were modeled by a pseudo-Voigt peak shape function, and the lattice dimensions, 1/x profile backdrop, zero error, scale factors, and four-coefficient Chebychev polynomial were all successively tuned.

Transmission electron microscopy (FEI Tecnai TF20: FEGTEM Field emission gun TEM/STEM equipped with HAADF detector) was used to characterize the surface topography and size of the undoped and rare earth ions doped nanostructures.

The apatite decomposition reactions and related phase transition during the heating of the materials in the air atmosphere were investigated using a simultaneous thermal analyzer (PerkinElmer®, STA 8000) equipped with thermogravimetric analysis (TGA) capacity. Every thermal experiment was conducted at a heating rate of 10 °C/min, with a temperature range of 30–1200 °C. For keeping the apatite mineral uncontaminated from the crucible material in STA, alumina crucible was chosen.

For vibrational spectroscopic analysis of apatite minerals, the Bruker Vertex 70 v FTIR spectrophotometer equipped with an attenuated total reflectance (ATR) head was employed for characterising the differences in the molecular vibrations in the apatite compositions.

The X-ray photoelectron spectroscopy experiments were performed on a SPECS Flex Mod UHV-XPS system at a pressure of around

**Table 1.** Materials synthesized for the investigation and their corresponding Ca/P ratio.

S.No.	Materials synthesized	Formula	Ca/P ratio
1.	FA (OH and Sr bearing)	$Ca_{4.98}Sr_{0.02}(PO_4)_3OH_{0.98}F_{0.02}$	1.66
2.	FA (OH and Sr bearing) Ce = 2 mole%	$Ca_{4.96}Sr_{0.02}Ce_{0.02}(PO_4)_3OH_{0.98}F_{0.02}$	1.65
3.	FA (OH and Sr bearing) Ce = 2 mole%, Sm = 1 mole%	$Ca_{4.95}Sr_{0.02}Ce_{0.02}Sm_{0.01}(PO_4)_3OH_{0.98}F_{0.02}$	1.65
4.	FA (OH and Sr bearing) Ce = 2 mole%, Ho and Sm = 1 mole%	$Ca_{4.94}Sr_{0.02}Ce_{0.02}Sm_{0.01}Ho_{0.01}(PO_4)_3OH_{0.98}F_{0.02}$	1.64

$1 \times 10^{-9}$  mbar. The system has a SPECS Phoibos 150 hemispherical analyzer with 1D delay line detectors and a SPECS XR-50 M Al anode X-ray source. The samples were measured in medium area mode with the slits fully open. The Al anode (1486.7 eV) was used at a power of 400 W and 15 kV with a spot size of 3.5 mm $\times$ 1 mm. Powdered samples were pressed lightly into pellets and attached to standard omicron sample plates via double-backed sticky tape. Samples were charge neutralized during measurement with an electron flood gun with a current of 75  $\mu$ A and an energy of 4 eV. Measurements were taken using SPECS lab Prodigy software and analyzed using CasaXPS.

## 2. Results and Discussion

### 2.1. Chemical and Structural Analysis

The XRD patterns of  $\text{Ca}_{4.96}\text{Sr}_{0.02}(\text{PO}_4)_3\text{OH}_{0.98}\text{F}_{0.02}$ ,  $\text{Ca}_{4.95}\text{Sr}_{0.02}\text{Ce}_{0.02}(\text{PO}_4)_3\text{OH}_{0.98}\text{F}_{0.02}$ ,  $\text{Ca}_{4.95}\text{Sr}_{0.02}\text{Ce}_{0.02}\text{Sm}_{0.01}(\text{PO}_4)_3\text{OH}_{0.98}\text{F}_{0.02}$  and  $\text{Ca}_{4.94}\text{Sr}_{0.02}\text{Ce}_{0.02}\text{Sm}_{0.01}\text{Ho}_{0.01}(\text{PO}_4)_3\text{OH}_{0.98}\text{F}_{0.02}$  (referred to as FA, FAcE, FAcEsm and FAcEsmHo, respectively) are shown in Figure 1(i).

The XRD patterns show fundamental diffraction peaks that were indexed with JCPDS no. 04–015–6661, indicating a hexagonal crystal structure ( $P6_3/m$  space group). Upon detailed structural analysis, a shift in the diffraction peaks towards a lower angle was observed, suggesting the substitution of rare earth ions in the lattice (as shown in Figure 1(ii)). This behaviour can be attributed to the difference in ionic radii between  $\text{Ca}^{2+}$

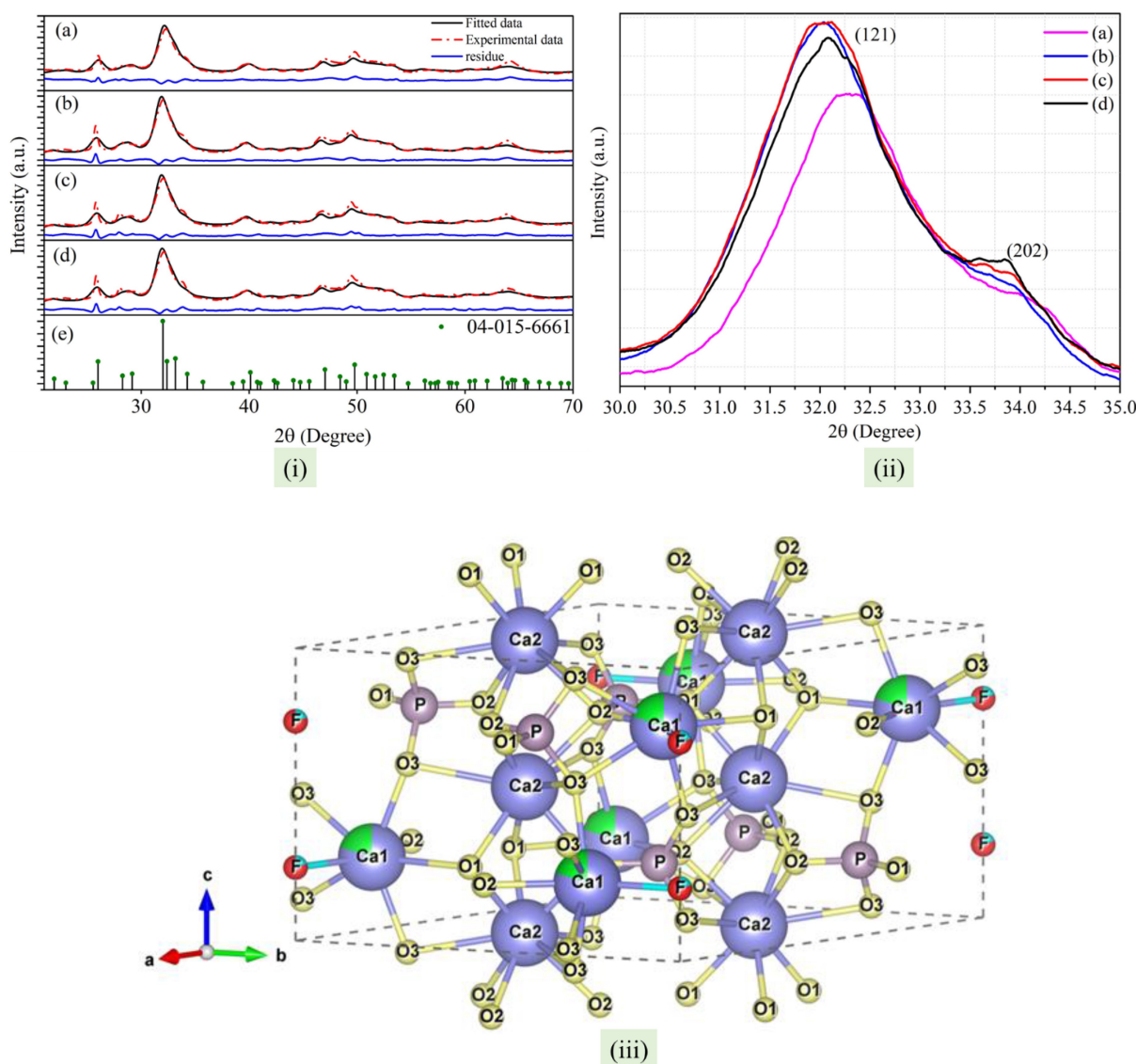


**Figure 1.** (i) The Rietveld refinement of the powder X-ray diffraction (PXRD) data carried out for room temperature XRD patterns for (a) FA; (b) FA: Ce; (c) FA: CeSm; (d) FA: CeSmHo; (ii) Enlarged XRD pattern of (a) FA; (b) FA: Ce; (c) FA: CeSm; (d) FA: CeSmHo. X-ray diffraction patterns indicate rare earth ion substitution, shown by peak shift to the lower angle. (iii) Typical schematic crystal structures of pristine fluorapatite for compositions FA.

(~1.06 Å) and rare earth ions such as Ce<sup>3+</sup> (1.15 Å), Sm<sup>3+</sup> (1.10 Å), and Ho<sup>3+</sup> (1.04 Å) ions.<sup>[18–20]</sup> Due to the solution processing method, the obtained particles might be very small and exhibit some amorphous characteristics. The assessment of crystallinity was performed using XRD data for the four compositions: FA, FA: Ce, FA: CeSm, and FA: CeSmHo, resulting in values of 85.41 %, 87.67 %, 90.42 %, and 87.37 %, respectively. The phosphate tetrahedra in the apatite compounds are linked to one another by cation polyhedra, which form quasi layer.<sup>[5]</sup> Typical schematic crystal structure of FA is shown in Figure 1(iii).

Figure 2(i) and (ii) present the results of morphological investigations of FA and FACeSm respectively. The rod-like morphology of formed particles is evident for both samples from TEM (Figure 2 (i) and (ii) a, b) and STEM images (Figure 2(i) and (ii) f, g). The dimensions of the rods are ~10 nm x 50 nm. The calculated value of d spacing, 0.36 nm and 0.38 nm for FA and FACeSm nanoparticles respectively correspond to (002) plane, obtained from the interplanar spacing of the lattice fringes in HRTEM images (Figure 2 (i) and (ii) d). Figures 2(i) and (ii) c display the polycrystalline selected area electron diffraction (SAED) pattern obtained from the nanorods. The elemental composition of formed samples is verified by Energy Dispersive X-ray Spectroscopy (EDX) (supplementary Figure S2(i–iv)). The presence of rare earth ions along with other elements in the EDX of doped FA confirm their effective doping in the apatite structure. The atomic percentages of various elements in the samples are in good agreement with that of the theoretically estimated one. The FTIR spectra of the prepared materials are shown in Figure S3(i)(ii) before and after heat treatment. Across all apatites, similar peaks corresponding to the PO<sub>4</sub><sup>3-</sup> ion bands are observed. Specifically, the  $\nu_4$  band is identified around 561 and 603 cm<sup>-1</sup>, and the  $\nu_1$  band around 965 cm<sup>-1</sup>. The highest peak, attributed to the  $\nu_3$  PO<sub>4</sub><sup>3-</sup> ion band, is found around

1020 cm<sup>-1</sup>. Additionally, the OH<sup>-1</sup> ion band is observed at approximately 3400 cm<sup>-1</sup>.<sup>[17]</sup> Formation of carbonates were not observed.

In the apatite structure there are two distinct cationic positions (4f and 6 h) having different coordination numbers and local symmetry.<sup>[5]</sup> The ionic radii of Ca<sup>2+</sup> cation, Ca<sub>I</sub> and Ca<sub>II</sub> sites are 1.06 Å and 1.18 Å<sup>[5]</sup> respectively. The Apatite structure has a distinct structural feature of accepting numerous isomorphous substitutions while still maintaining its hexagonal space group *P6<sub>3</sub>/m*. The preferred site for Sr substitution is Ca<sub>I</sub>, as it only marginally distorts site I coordination configuration at lower concentrations and is energetically more favorable than mixed sites or site II.<sup>[21,22]</sup> The cerium and samarium ions prefer the Ca<sub>II</sub> position whereas the holmium ion prefers Ca<sub>I</sub> position to balance the bond valence of Ca.<sup>[20]</sup> The Rietveld refinement was used to analyze the powder diffraction data of the samples from 25–500 °C. The Rietveld refinement of PXRD data of FA, FACe, FACeSm and FACeSmHo was performed at (a) 100 °C; (b) 200 °C; (c) 300 °C; (d) 400 °C; (e) 500 °C (supplementary Figure S1). The lattice parameters obtained for FA, FACe, FACeSm, and FACeSmHo from RT to 500 °C are shown in Table 2, 3, 4 and 5 respectively. The RT lattice parameters of the prepared materials were found to increase with an increasing number of dopant ions may be due to the increasing number of ions getting accommodated to these sites. The refinement parameters for all the compositions at RT are shown in table ST1 in the supplementary section.

## 2.2. Influence of Ca/P Ratio on the Thermal Stability of Apatite

A useful and popular method for analyzing materials undergoing structural changes and phase transitions that take place

**Table 2.** The lattice parameters of FA from RT to 500 °C.

Temperature [°C]	a [Å]	$\alpha_a \times 10^6$ , [K <sup>-1</sup> ]	c [Å]	$\alpha_c \times 10^6$ , [K <sup>-1</sup> ]	V [Å <sup>3</sup> ]
RT	9.411(3)	6.6	6.890(1)	12.1	528.513(2)
100 °C	9.421(1)		6.895(3)		529.890(2)
200 °C	9.430(1)		6.902(2)		531.584(1)
300 °C	9.435(4)		6.905(1)		532.423(3)
400 °C	9.441(3)		6.920(1)		534.232(2)
500 °C	9.447(2)		6.931(2)		535.670(1)

**Table 3.** The lattice parameters of FACe from RT to 500 °C.

Temperature [°C]	a [Å]	$\alpha_a \times 10^6$ , [K <sup>-1</sup> ]	b [Å]	$\alpha_c \times 10^6$ , [K <sup>-1</sup> ]	V [Å <sup>3</sup> ]
RT	9.430(1)	8.9	6.900(1)	12.1	531.381(3)
100 °C	9.440(3)		6.906(1)		533.032(1)
200 °C	9.453(3)		6.910(2)		534.880(3)
300 °C	9.463(1)		6.917(1)		536.424(2)
400 °C	9.468(2)		6.931(3)		538.062(1)
500 °C	9.478(3)		6.940(1)		540.014(4)

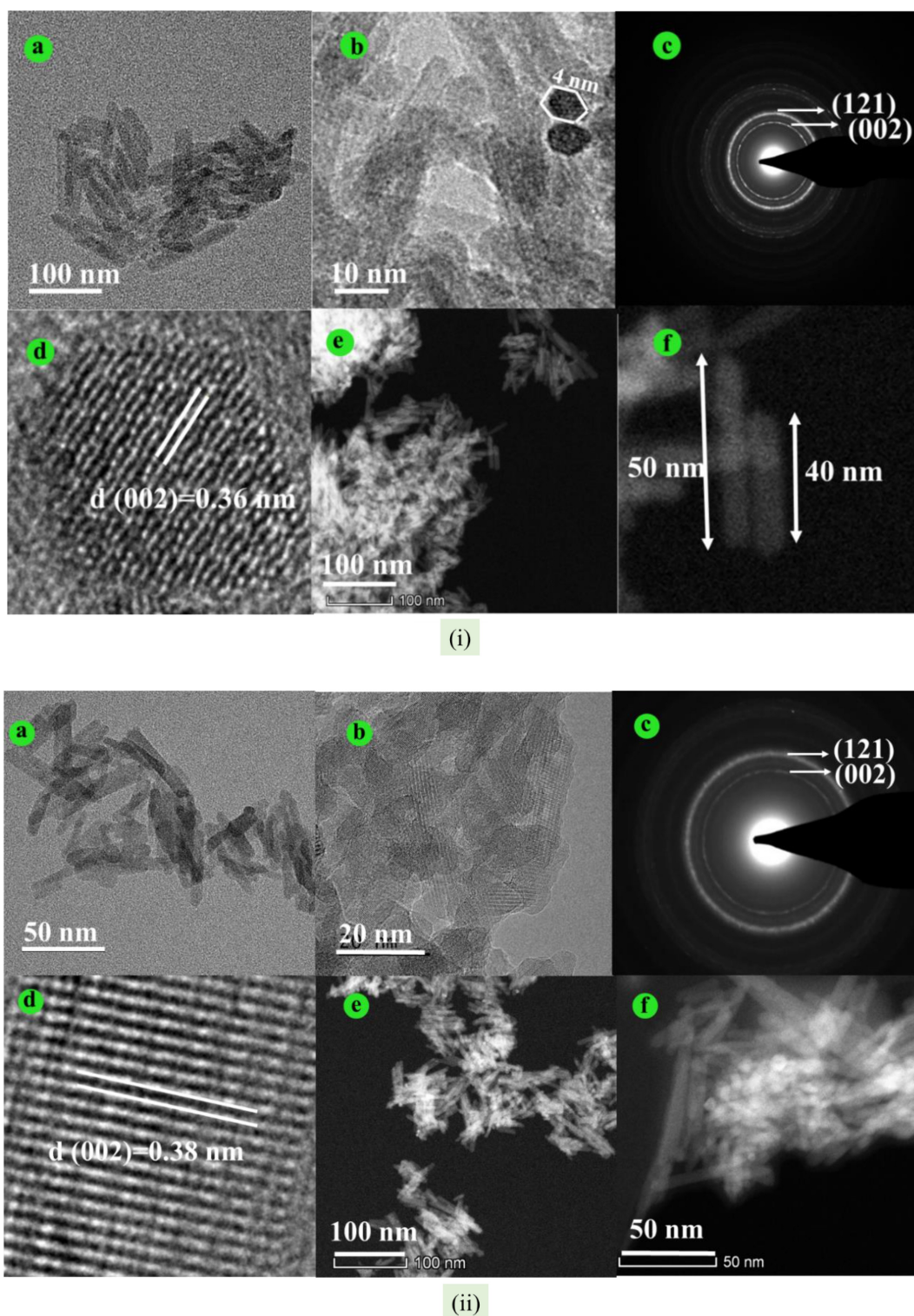


**Figure 2.** (i): (a), (b) TEM images indicating rod shaped particles are produced; (c) SAED diffraction pattern indicates polycrystallinity in the nanoparticles; (d) HRTEM image shows the lattice fringes; (e), (f) STEM images of undoped FA nanoparticles. (ii): (a), (b) TEM images; (c) SAED diffraction pattern; (d) HRTEM image; (e), (f) STEM images of undoped FACeSm nanoparticles. The rod-shaped particles with a polycrystalline nature were produced.

inside a material when it is exposed to high temperature is *in situ* high-temperature X-ray diffraction.<sup>[8,10–15]</sup> The thermal stability of the apatite structure is dependent on the Ca/P ratio, with any deviation from the stoichiometric value (1.667)

influencing its thermal stability.<sup>[14]</sup> High-temperature treatment of these materials leads to the annealing of defects, accompanied by an increase in crystallite size, ultimately resulting in the formation of stoichiometric apatite crystallites.

**Table 4.** The lattice parameters of FAcEsm from RT to 500 °C.

Temperature [°C]	a [Å]	$\alpha_a \times 10^6$ , [K <sup>-1</sup> ]	b [Å]	$\alpha_c \times 10^6$ , [K <sup>-1</sup> ]	V [Å <sup>3</sup> ]
RT	9.430(1)	11.1	6.880(1)	18.2	529.860(1)
100 °C	9.435(3)		6.887(3)		530.941(3)
200 °C	9.443(2)		6.900(2)		532.844(1)
300 °C	9.449(4)		6.909(1)		534.192(2)
400 °C	9.459(1)		6.919(2)		536.690(4)
500 °C	9.479(2)		6.941(1)		540.213(2)

**Table 5.** The lattice parameters of FAcEsmHo from RT to 500 °C.

Temperature [°C]	a [Å]	$\alpha_a \times 10^6$ , [K <sup>-1</sup> ]	b [Å]	$\alpha_c \times 10^6$ , [K <sup>-1</sup> ]	V [Å <sup>3</sup> ]
RT	9.440(2)	6.6	6.870(1)	15.2	530.220(1)
100 °C	9.443(5)		6.881(1)		531.433(2)
200 °C	9.455(1)		6.891(3)		533.532(3)
300 °C	9.466(2)		6.910(2)		536.342(2)
400 °C	9.473(3)		6.922(3)		537.910(1)
500 °C	9.477(3)		6.944(2)		539.724(3)

In instances where there is an absence or imbalance of calcium or phosphate ions ( $\text{Ca/P} \neq 1.667$ ), the apatite structure tends to decompose, giving rise to its stoichiometric form and impurity phases.<sup>[14]</sup> Apatite exhibiting calcium deficiency ( $\text{Ca/P} = 1.6$ ) tends to form the  $\text{Ca}_3(\text{PO}_4)_2$  phase, whereas an excess of calcium cations ( $\text{Ca/P} = 1.7$ ) typically leads to the formation of CaO following high-temperature sintering. In our study, non-stoichiometric apatites were prepared, varying the Ca/P ratio from 1.66–1.64 in FA to FAcEsmHo. The specific Ca/P ratios for the synthesized materials are detailed in Table 1. The atomic percentages obtained from EDX (supplementary figure S2(i)–(iv)) are also in close agreement with the theoretically estimated value. The Ca/P ratio obtained from EDX for FA, FAcE, FAcEsm and FAcEsmHo is also found to decrease from 1.66 to 1.64.

The temperature dependency of the crystal structure parameters (atomic coordinates, bond lengths, bond angles, etc.) and the lattice characteristics (unit cell parameters, interplanar spacings) can be used to characterize the crystal's thermal expansion. A quantitative measure of thermal deformation (thermal expansion) is the thermal expansion coefficient. The apatite family has large thermal expansion coefficients.<sup>[23]</sup> Rise in temperature causes crystals to distort. The thermal expansion coefficient is most commonly used to explain thermal fluctuations in the unit cell characteristics and the unit cell volume. The thermal expansion characteristics of hexagonal phases were investigated by examining the temperature dependencies of their unit cell parameters, as outlined in Table 2–5. These parameters were subjected to fitting procedures using linear or quadratic equations. Notably, the unit cell parameters and the volume exhibited a compatibility with linear fitting, might be due to the presence of rare earth ions and fluorine in the lattice (Figure S4(i)–(iii)). Equation (1) shows the relationship between the change in temperature and the thermal expansion coefficient ( $\alpha_a$ ).

$$\alpha_a = \left(\frac{1}{a}\right) \left(\frac{da}{dT}\right) \quad (1)$$

The thermal expansion coefficients (TECs) were investigated for FA, FAcE, FAcEsm, and FAcEsmHo along the crystallographic "a" and "c" axes up to 500 °C. Table 2–5 documents these TEC values. The introduction of cerium ions into the  $\text{Ca}_{\text{II}}$  lattice site leads to a noticeable expansion along the "a" crystallographic axis. However, the impact on the "c" axis expansion is negligible, indicating anisotropic thermal expansion behaviour. When samarium ions are additionally introduced into the  $\text{Ca}_{\text{II}}$  lattice site along with cerium, the unit cell undergoes expansion in both the "a" and "c" directions. This suggests a synergistic effect of cerium and samarium doping on the lattice expansion. Interestingly, the inclusion of holmium ions in the  $\text{Ca}_{\text{I}}$  lattice site of the triple-doped material results in a reduction of the thermal expansion coefficient. This reduction can be attributed to the comparatively smaller size of holmium ions, leading to a shrinkage in the overall lattice volume. It is plausible that this shrinkage effect is counterbalanced by the presence of cerium and samarium ion doping, which tends to promote an overall expansion in the lattice structure.

The investigation revealed a distinctive anisotropic behaviour in the lattice expansion of the prepared samples, with increased sensitivity along the "c" crystallographic axis. This phenomenon stems from non-uniform changes in lattice parameters in different directions and can be ascribed to various underlying factors, one of which pertains to the relative strength of chemical bonds along specific crystallographic axes. The spatial arrangement of  $\text{PO}_4^{3-}$  tetrahedral units within the unit cell warrants consideration. These tetrahedral units are organized in sets of three, adopting a distinctive "pinwheel" configuration around the central  $\text{Ca}_{\text{II}}$  ion. This unique geometric disposition imparts distinct mechanical responses along various

crystallographic axes, thus contributing to the observed anisotropic behavior.<sup>[8]</sup>

Upon heating beyond 500 °C, the synthesized materials undergo phase transformation. The details of phase transformations at different temperatures are illustrated in Figure 3–7. Figure 3 and Figure 7 (a) show the XRD patterns and TGA-DSC curve of FA respectively. The *in situ* XRD at 600 °C shows a phase separation in the material with the formation of two distinct phases. The identified compositions are likely  $\text{Ca}_{9.37}\text{Sr}_{0.63}(\text{PO}_4)_6(\text{OH})_{0.98-2x}\text{F}_{0.02}\text{O}_x$  and  $\text{Sr}_{7.3}\text{Ca}_{2.7}(\text{PO}_4)_6(\text{OH})_{0.98-2x}\text{F}_{0.02}\text{O}_x$  because of close agreement of the XRD data with  $\text{Ca}_{9.37}\text{Sr}_{0.63}(\text{PO}_4)_6\text{F}_2$  (ICDD-01-079-1459) and  $\text{Sr}_{7.3}\text{Ca}_{2.7}(\text{PO}_4)_6(\text{OH})\text{F}_2$  (ICDD-01-078-1715). The phase transformation continues at 720 °C with increasing amounts of oxyapatites being formed at higher temperatures. As can be seen from Figure 7(a), the loss of adsorbed water was the primary source of the weight loss, which occurred when the temperature was raised from room temperature to 130 °C. Weight loss of around 7.6% was observed in the temperature range of 130–585 °C due to removal of lattice water. The weight loss of 1.17% further continued till 720 °C. In the range of 800–1000 °C, the oxyapatites decomposed into  $\beta$ -tricalcium phosphate. The increasing amount of  $\beta\text{Ca}_3(\text{PO}_4)_2$  (mp-531132) was formed between 800–1000 °C (as observed from the XRD pattern). When the temperature was above 1000 °C,  $\beta\text{Ca}_3(\text{PO}_4)_2$  reacted with oxyapatite to form  $\alpha\text{Ca}_3(\text{PO}_4)_2$  (mp-1197377). During the cooling process the  $\alpha\text{Ca}_3(\text{PO}_4)_2$  reacted with  $\text{Ca}_{9.37}\text{Sr}_{0.63}(\text{PO}_4)_6(\text{OH})_{0.98-2x}\text{F}_{0.02}\text{O}_x$  to form  $(\text{Ca}_{9.98}\text{Sr}_{0.02}(\text{PO}_4)_6(\text{OH})_2$  (ICDD-01-077-9004) and  $\text{Sr}_{7.3}\text{Ca}_{2.7}(\text{PO}_4)_6\text{F}_2$  (ICDD-01-078-1715) and small amount of  $\text{Ca}_3(\text{PO}_4)_2$  (mp-753711), which is slightly more dense form of  $\alpha\text{Ca}_3(\text{PO}_4)_2$ .

Upon the addition of rare earth ions to the apatite structure, the decomposition behaviour changed slightly. Figure 4 and Figure 7(b) show the XRD patterns (from 600 °C to 1200 °C) and TGA-DTA curve FAcE respectively.

FAcE phase separates at 600 °C leading to the formation of two different apatites  $\text{Ca}_{9.37}\text{Sr}_{0.63}(\text{PO}_4)_6(\text{OH})_{0.98-2x}\text{F}_{0.02}\text{O}_x$  and  $\text{Sr}_{7.3}\text{Ca}_{2.7}(\text{PO}_4)_6(\text{OH})_{0.98-2x}\text{F}_{0.02}\text{O}_x$ . Figure 7(b) shows that when the temperature was raised from room temperature to 130 °C, the sample lost approximately 4.22% of its weight due to the loss of adsorbed water. The reduced amount of water loss observed in comparison to FA might be due to the presence of the lesser amount of adsorbed water in FAcE in comparison to FA (also evident in FTIR analysis (supplementary Figure S5(ii)). In the temperature range of 130–585 °C, lattice water was lost leading to a weight loss of approximately 8.82%. The incorporation of cerium ions might be causing instability in the structure. The weight loss of 0.8% was observed further till 740 °C. The weight loss has decreased in this region might be due to the interaction of cerium ions with OH which decelerates the weight loss process. An increasing amount of  $\beta\text{Ca}_3(\text{PO}_4)_2$  was formed between 800–1000 °C (as observed from the XRD pattern) due to the decomposition of oxyapatites. When the reaction temperature was above 1000 °C,  $\beta\text{Ca}_3(\text{PO}_4)_2$  reacts with oxyapatites to form  $\alpha\text{Ca}_3(\text{PO}_4)_2$ . During the cooling process the  $\alpha\text{Ca}_3(\text{PO}_4)_2$  reacted with  $\text{Ca}_{9.37}\text{Sr}_{0.63}(\text{PO}_4)_6(\text{OH})_{0.98-2x}\text{F}_{0.02}\text{O}_x$  to form stoichiometric apatites  $(\text{Ca}_{9.98}\text{Sr}_{0.02}(\text{PO}_4)_6(\text{OH})_2$  and  $\text{Sr}_{7.3}\text{Ca}_{2.7}(\text{PO}_4)_6\text{F}_2$  and considerable amount of  $\beta\text{Ca}_3(\text{PO}_4)_2$ .

With the addition of samarium ions to FAcE in FAcESm, the adsorbed water loss was found to be 5.35% when the temperature changed to 125 °C, which is comparable to FAcE (Figure 7(c)). It is observed from Figure 5, FAcESm phase separated

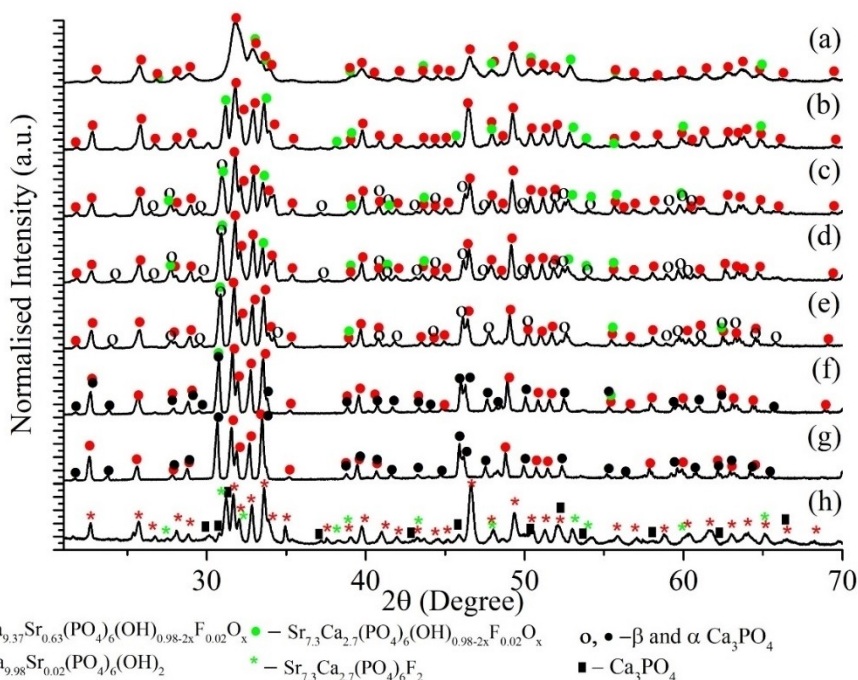


**Figure 3.** The XRD pattern of FA at various temperatures: a) 600 °C, b) 700 °C, c) 800 °C, d) 900 °C, e) 1000 °C, f) 1100 °C, g) 1200 °C; h) room temperature after cooling. After cooling to RT small amount of  $\text{Ca}_3(\text{PO}_4)_2$  is formed along with stoichiometric apatites.

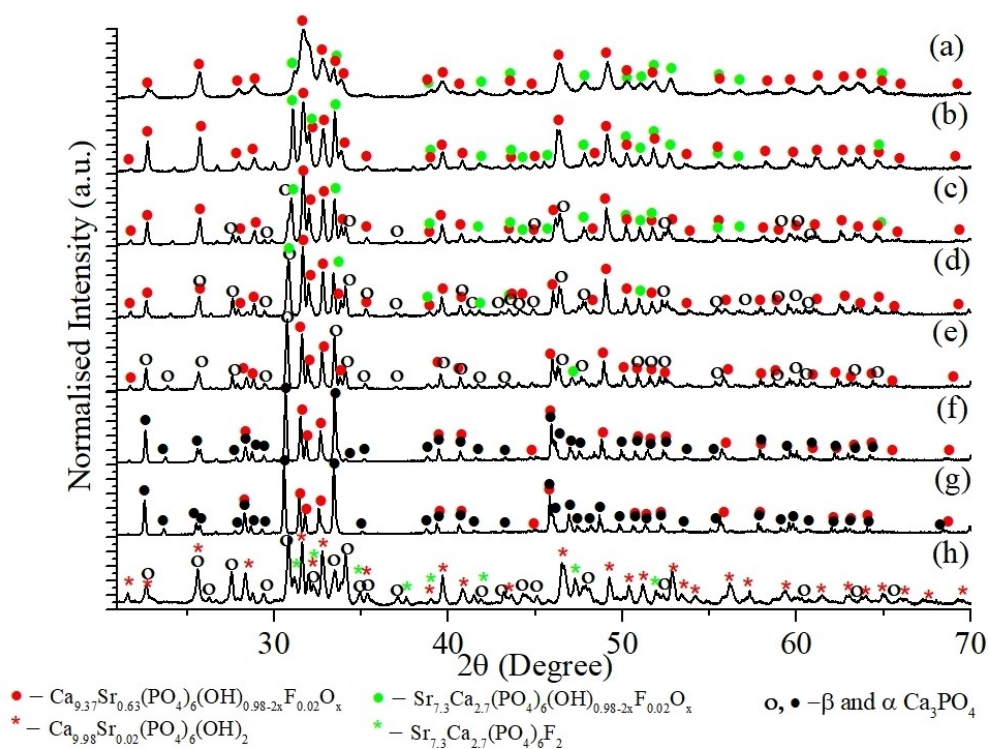


**Figure 4.** The XRD pattern of FACe at various temperatures: a) 600 °C, b) 700 °C, c) 800 °C, d) 900 °C, e) 1000 °C, f) 1100 °C, g) 1200 °C; h) room temperature after cooling.

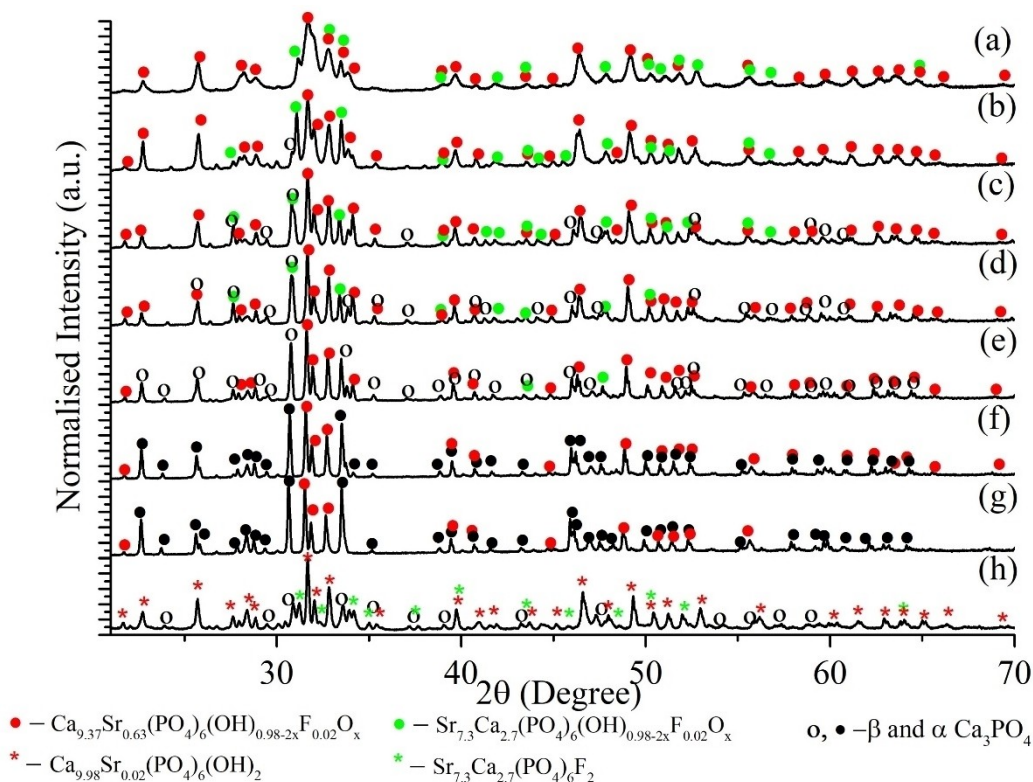


**Figure 5.** The XRD pattern of FACeSm at various temperatures: a) 600 °C, b) 700 °C, c) 800 °C, d) 900 °C, e) 1000 °C, f) 1100 °C, g) 1200 °C; h) room temperature after cooling.

at 600 °C leading to the formation of two different apatites  $\text{Ca}_{9.37}\text{Sr}_{0.63}(\text{PO}_4)_6(\text{OH})_{0.98-2x}\text{F}_{0.02}\text{O}_x$  and  $\text{Sr}_{7.3}\text{Ca}_{2.7}(\text{PO}_4)_6(\text{OH})_{0.98-2x}\text{F}_{0.02}\text{O}_x$ . The loss of lattice water between 130–543 °C lead to weight loss of 1.49%. The weight loss of 0.16% was observed further till 770 °C. The decomposition of oxyapatites took place at a much lower temperature (600–700 °C) in comparison to FA and FAcE might be due to the instability caused by rare earth ions in the lattice. An increasing amount of  $\beta\text{Ca}_3(\text{PO}_4)_2$  was formed between 700–1000 °C (as observed from the XRD pattern) due to the decomposition of oxyapatites. When the temperature was above 1000 °C,  $\beta\text{Ca}_3(\text{PO}_4)_2$  reacted with oxyapatites to form  $\alpha\text{Ca}_3(\text{PO}_4)_2$ . During the cooling process the  $\alpha\text{Ca}_3(\text{PO}_4)_2$  reacts with  $\text{Ca}_{9.37}\text{Sr}_{0.63}(\text{PO}_4)_6(\text{OH})_{0.98-2x}\text{F}_{0.02}\text{O}_x$  to form stoichiometric apatites  $(\text{Ca}_{9.98}\text{Sr}_{0.02}(\text{PO}_4)_6(\text{OH})_2$  and  $\text{Sr}_{7.3}\text{Ca}_{2.7}(\text{PO}_4)_6\text{F}_2$  and considerable amount of  $\beta\text{Ca}_3(\text{PO}_4)_2$ .

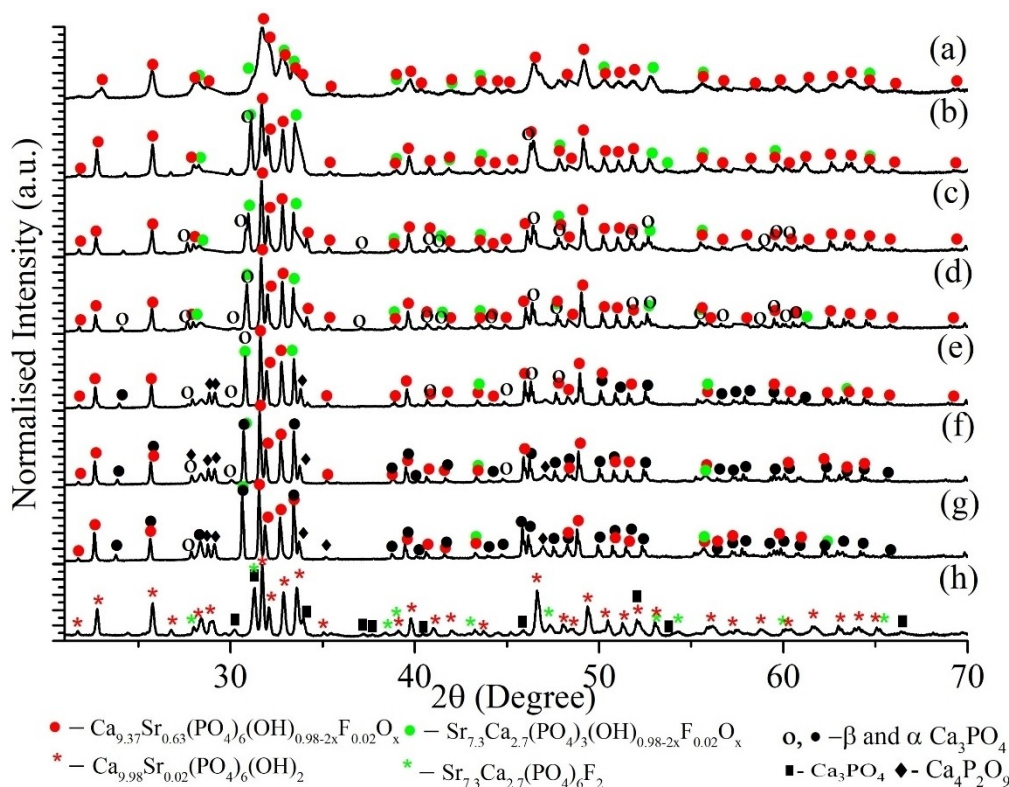
It can be seen from Figure 6 and 7 (d) that the increasing amount of rare earth ions is making the apatite structure unstable. The adsorbed water loss was found to be minimal for FAcEsmHo (4.11%) when the temperature changes to 125 °C. The loss of lattice water happened in the temperature range of 130–580 °C and the weight loss was found to be about 3.87%. The weight loss of 0.54% was observed further till 770 °C.

The decomposition of oxyapatites took place at a much lower temperature (600–700 °C), which might be due to the instability caused by rare earth ions in the lattice. An increasing amount of  $\beta\text{Ca}_3(\text{PO}_4)_2$  was formed between 700–900 °C (as observed from the XRD pattern) due to the decomposition of

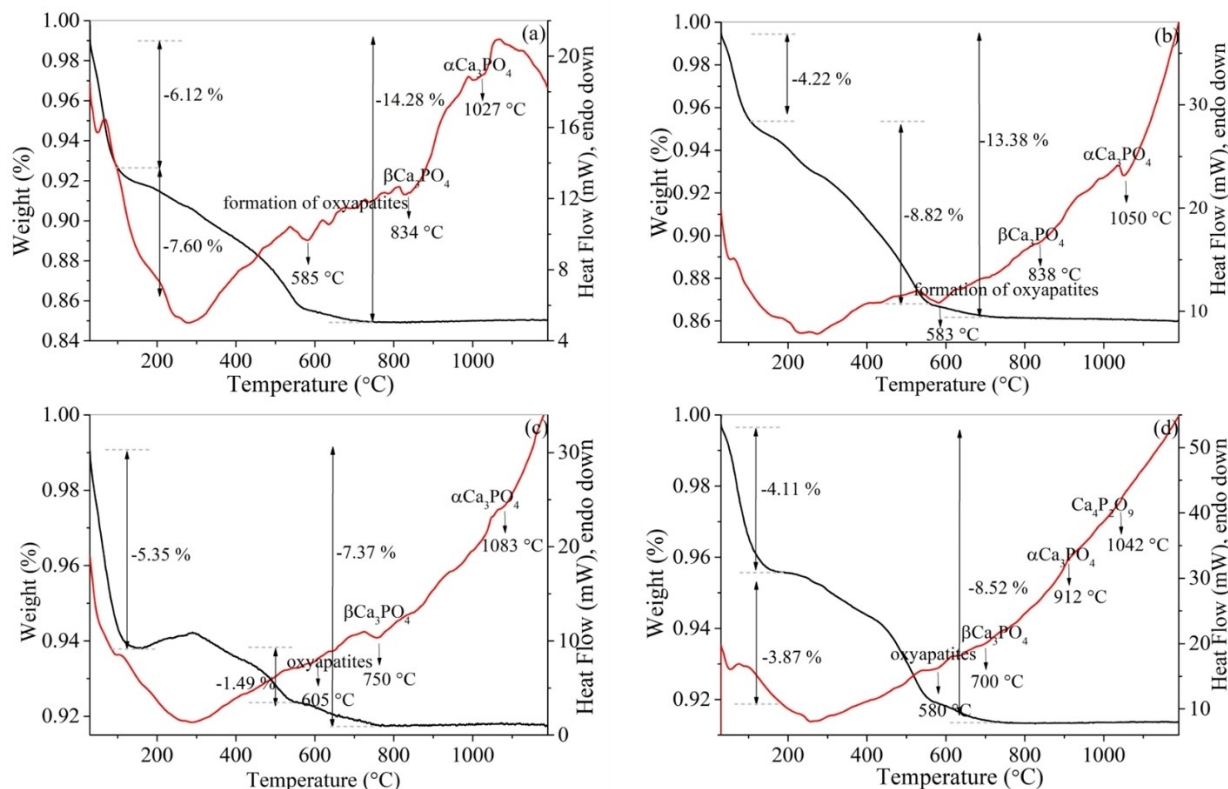
oxyapatites. Around 1000 °C,  $\beta\text{Ca}_3(\text{PO}_4)_2$  reacted with oxyapatite to form  $\alpha\text{Ca}_3(\text{PO}_4)_2$ . Between 1000–1200 °C, the oxyapatite further decomposed to  $\alpha\text{Ca}_3(\text{PO}_4)_2$ ,  $\beta\text{Ca}_3(\text{PO}_4)_2$  and  $\text{Ca}_4\text{P}_2\text{O}_9$  existed along with oxyapatites. The  $\alpha\text{Ca}_3(\text{PO}_4)_2$  phosphate was formed at a much lower temperature in FAcEsmHo in comparison to the other materials synthesized. The rare earth ions have different sizes than the calcium sites which creates stress in the lattice leading to slightly different decomposition pathways. During the cooling process the  $\alpha\text{Ca}_3(\text{PO}_4)_2$  reacted with  $\text{Ca}_{9.37}\text{Sr}_{0.63}(\text{PO}_4)_6(\text{OH})_{0.98-2x}\text{F}_{0.02}\text{O}_x$  to form stoichiometric apatites  $(\text{Ca}_{9.98}\text{Sr}_{0.02}(\text{PO}_4)_6(\text{OH})_2$  and  $\text{Sr}_{7.3}\text{Ca}_{2.7}(\text{PO}_4)_6\text{F}_2$  and a small amount of  $\text{Ca}_3(\text{PO}_4)_2$ . The comparison of phase transformations of all the samples prepared is shown in Figure 8.

Figure 9 displays the TEM results of FAcEsm samples after heat treatment. Figures 9 (a) and (b) indicate growth in the crystallite size after heat treatment, and the particles with distorted morphology and a size of approximately 200 nm were formed. Furthermore, the high-resolution TEM image of the formed particles displays lattice fringes from both  $(\text{Sr}_{7.3}\text{Ca}_{2.7})(\text{PO}_4)_6\text{F}_2$  and  $\text{Ca}_{9.98}\text{Sr}_{0.02}(\text{PO}_4)_6(\text{OH})_2$  as shown in Figure 9(c). These particles exhibit high crystallinity, and the ring pattern was indexed to  $\text{Ca}_{9.98}\text{Sr}_{0.02}(\text{PO}_4)_6(\text{OH})_2$ . Additionally, the SAED pattern confirmed the presence of  $\beta\text{Ca}_3(\text{PO}_4)_2$  in the heat-treated sample. XRD and TEM results are in good agreement with each other.

Figure 10, S5 (i) and (ii) show a comparison between the FTIR spectra of heat-treated and pristine FA, FAcE, FAcEsm, and FAcEsmHo nanoparticles. The asymmetric bending vibration of



**Figure 6.** The XRD pattern of FAcEsmHo at various temperatures: a) 600 °C, b) 700 °C, c) 800 °C, d) 900 °C, e) 1000 °C, f) 1100 °C, g) 1200 °C; h) room temperature after cooling.



**Figure 7.** (a) TGA and DSC curves for FA. The formation of oxyapatites,  $\beta\text{Ca}_3\text{PO}_4$  and  $\alpha\text{Ca}_3\text{PO}_4$  is observed around 585 °C, 834 °C and 1027 °C respectively; (b) TGA and DSC curves for FAcE; (c) TGA and DSC curves for FAcESm; (d) TGA and DSC curves for FAcESmHo. The loss of adsorbed water is the least in FAcESmHo compared to FA, FAcE, and FAcESm samples.

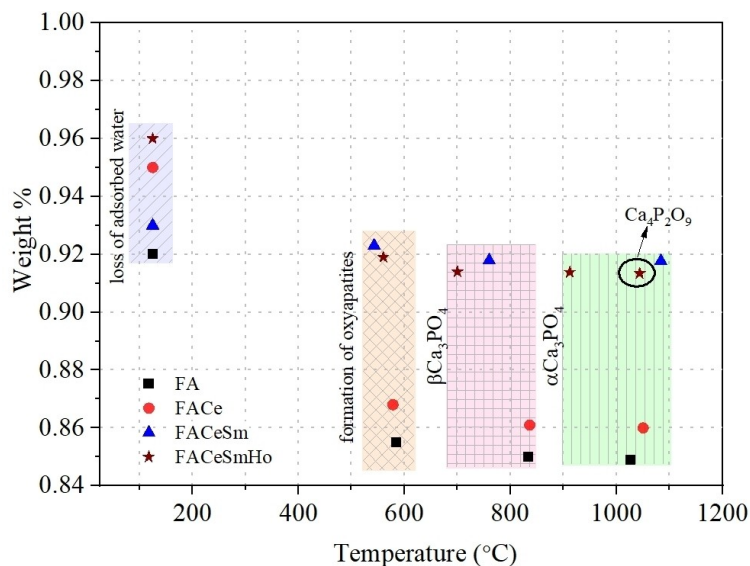


**Figure 8.** Comparison of phase transformation of FA, FAcE, FAcESm, FAcESmHo as a function of temperature. Apatite structures tend to opt for slightly different pathways for phase decomposition in the presence of rare earth ions.

the  $\text{PO}_4^{3-}$  group were observed at  $603\text{ cm}^{-1}$  and  $567\text{ cm}^{-1}$  (supplementary Figure S5 (i)). The peaks observed at  $1037\text{ cm}^{-1}$  and  $1092\text{ cm}^{-1}$  corresponded to the antisymmetric stretching vibration of the  $\text{PO}_4^{3-}$  group, while the peak at  $962\text{ cm}^{-1}$  was

attributed to the symmetry stretching vibration of the  $\text{PO}_4^{3-}$  group (Figure 10). Additionally, the stretching and bending vibrations of  $\text{OH}^-$  groups within the apatite structure were

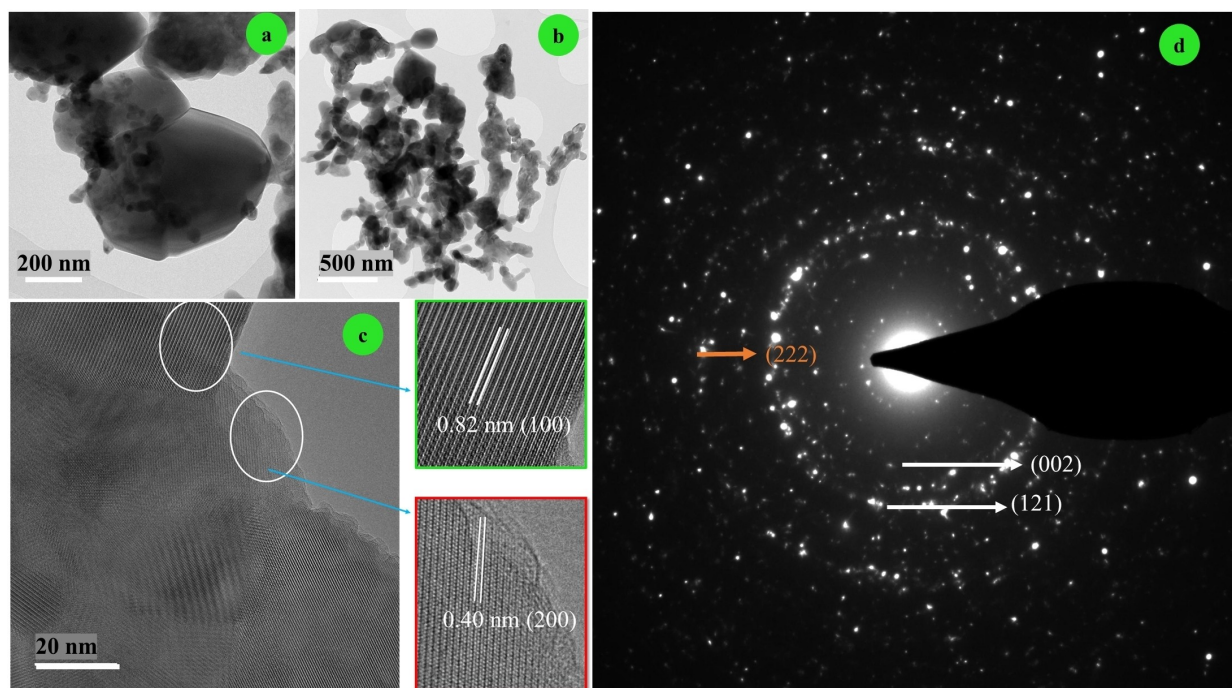


**Figure 9.** TEM images of FACeSm after being heat treated at 1200 °C are shown in (a) and (b). The particles show significant grain growth due to the heat treatment. A high-resolution TEM image of the nanoparticles after heat treatment is shown in (c). The HRTEM analysis revealed the presence of lattice fringes from  $(\text{Sr}_{7.3}\text{Ca}_{2.7})(\text{PO}_4)_6\text{F}_2$  (marked in green) as well as lattice fringes from  $\text{Ca}_{9.98}\text{Sr}_{0.02}(\text{PO}_4)_6(\text{OH})_2$  (marked in red). The particles formed are highly crystalline, as observed from the well-defined ring pattern in the selected area electron diffraction pattern (d). The rings can be indexed to  $\text{Ca}_{9.98}\text{Sr}_{0.02}(\text{PO}_4)_6(\text{OH})_2$  (marked in white), and the presence of tricalcium phosphate is also observed (marked in orange).

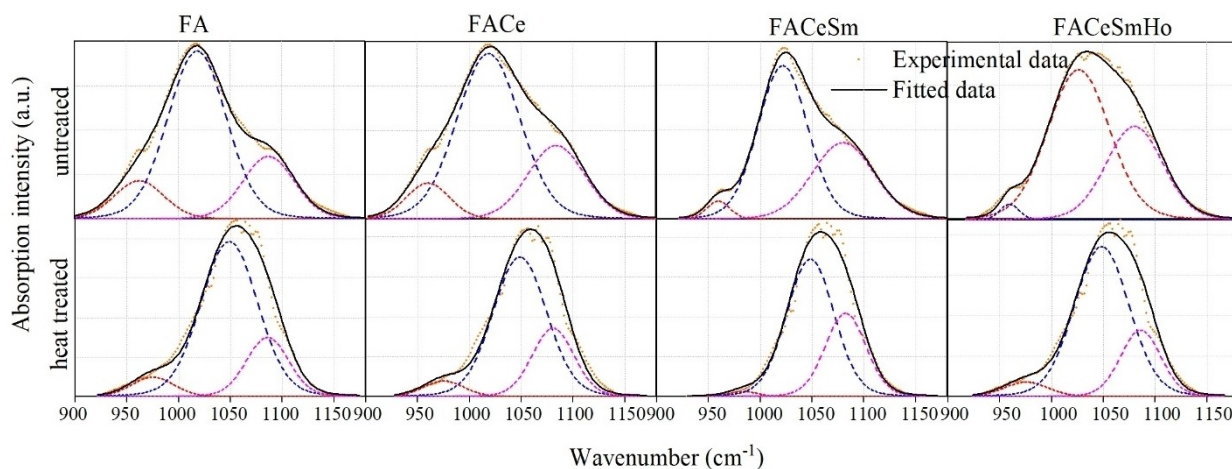


**Figure 10.** Comparison between the FTIR spectra of heat-treated and pristine FA, FACe, FACeSm, and FACeSmHo nanoparticles. The stretching vibrations of  $\text{PO}_4^{3-}$  ions are shifted to higher wavenumbers due to increased strain in the crystals caused by rare earth ions.

identified at approximately  $3572\text{ cm}^{-1}$  and  $635\text{ cm}^{-1}$ , respectively<sup>[24,25]</sup> (supplementary Figure S5(ii)).

Figure 10 depicts that as rare earth ions were incorporated into the apatite structure (from FA to FACeSmHo), the stretching vibrations of  $\text{PO}_4^{3-}$  ion ( $962\text{ cm}^{-1}$ ,  $1037\text{ cm}^{-1}$  and  $1092\text{ cm}^{-1}$ ) shifted to higher wavenumbers. This shift can be attributed to the increased strain in the crystals caused by rare earth ions, which alters the local electric field environment around  $\text{PO}_4^{3-}$  ions. After undergoing heat treatment, the vibrational bands of  $\text{PO}_4^{3-}$  ions became narrow and shifted

towards lower wavenumbers. This indicates the formation of stoichiometric apatite with improved crystallinity. The presence of tricalcium phosphate can be confirmed from the additional bands that appear around  $560\text{ cm}^{-1}$  and  $593\text{ cm}^{-1}$  in the spectra after heat treatment in figure S5(i) in the supplementary section.<sup>[25]</sup>

The intensity of the adsorbed  $\text{OH}^-$  band from FA to FACeSmHo was reduced by the presence of rare earth ions (supplementary Figure S5(ii)). The increased amount of rare earth ions tends to make the crystal surface more electro-

negative, which leads to the unavailability of electrons for the hybridization of  $\text{OH}^-$  ions. As a result, the hydration layer intensity decreases in rare earth ion-doped FAs.

X-ray photoelectron spectroscopy (XPS) was employed for surface composition analysis. A representative survey XPS spectrum was performed for both heated and unheated samples (supplementary Figure S6, S7). The spectra exhibit expected peaks corresponding to Ca, P, and O elements. Notably, a small C 1s peak is consistently observed in all tested samples, attributed to "adventitious carbon." This carbon presence, stemming from impurity hydrocarbon adsorption, was utilized for binding energy calibration. To address sample charging, the binding energy of adventitious carbon was set at 284.6 eV.<sup>[26]</sup> Additionally, the survey spectrum reveals the presence of rare earth ions cerium, samarium, and holmium, in the analyzed samples.

The apatite crystallizes into a hexagonal system with the space group  $P6_3/m$ . It features an almost compact assembly of phosphate ions ( $\text{PO}_4^{3-}$ ) and two types of tunnels. The tunnel I is wider and has a symmetry of 6h, with cations in site I and a coordination number of seven. Tunnel II is narrow and has a symmetry 4f, containing cations localized in site II, with a coordination number of nine.<sup>[27]</sup> High-resolution X-ray photoelectron spectroscopy (XPS) was utilized to analyze individual peaks. Figure 11 illustrates the high-resolution XPS spectra of Ca 2p for all samples, both before and after heat treatment. Within each spectrum, the distinct contributions of Ca  $2p_{3/2}$  and Ca  $2p_{1/2}$  are discernible. The measured spin-orbit splitting  $\delta(\text{Ca } 2p_{3/2} - \text{Ca } 2p_{1/2})$  is  $3.5 \pm 0.2$  eV for the various compounds.<sup>[28]</sup> The peaks of Ca  $2p_{3/2}$  for the as-synthesized FA, FACe, FACeSm, and FACeSmHo were observed at 347.3 eV, 347.1 eV, 347.2 eV, and 347.0 eV, respectively (Figure 11). This peak can be attributed to calcium bonds characteristic of apatite and calcium binding

with carbonate due to carbon species adsorbed from air. A slight variation in the binding energy value is observed with an increasing number of rare earth ions. After heat treatment, the Ca  $2p_{3/2}$  and Ca  $2p_{1/2}$  envelopes became broad. The peaks were deconvoluted into two peaks (peak I and peak II) shown in Figure 11. The binding energy values of the peaks fitted are listed in supplementary Table ST2. Peak I can be assigned to Ca coordination to the OH group of apatite structure and carbonate group due to carbon species adsorbed on the surface, while peak II can be assigned to coordination with the phosphate group of tri-calcium phosphate.<sup>[29]</sup>

The XPS spectra of the O 1s envelope of the synthesized samples were analyzed and fitted with three distinct peaks (supplementary Figure S8). The oxygen binding energy from the  $(\text{OH})^-$  groups of the apatite structure is represented by peak I, which is centered at 531.4 eV. The oxygen binding energy from the  $(\text{PO}_4)^{3-}$  of the apatite structure is represented by peak II, which is centered at 532.4 eV. The oxygen of adsorbed water on the apatite surface is responsible for peak III, which is centered at 533.4 eV. Following heat treatment, the oxygen binding energy from the  $(\text{OH})^-$  groups of the apatite structure was found to be centered at (i) 531.35 eV, and the oxygen binding energy from the  $(\text{PO}_4)^{3-}$  of the apatite structure was found to be centered at (ii) 532.3 eV (supplementary Table ST3). The peak corresponding to the oxygen of adsorbed water on the apatite surface disappeared after heat treatment. There is a slight variation in the peak positions of peaks I, II, and III with the increasing number of rare earth ions in the apatite structure. The analysis of the P 2p envelope (supplementary Figure S9) revealed P  $2p_{3/2}$  component at 132.6 eV, attributed to the P–O bonds of the apatite. Following heat treatment, a slight shift in the binding energy occurred, indicating changes in the

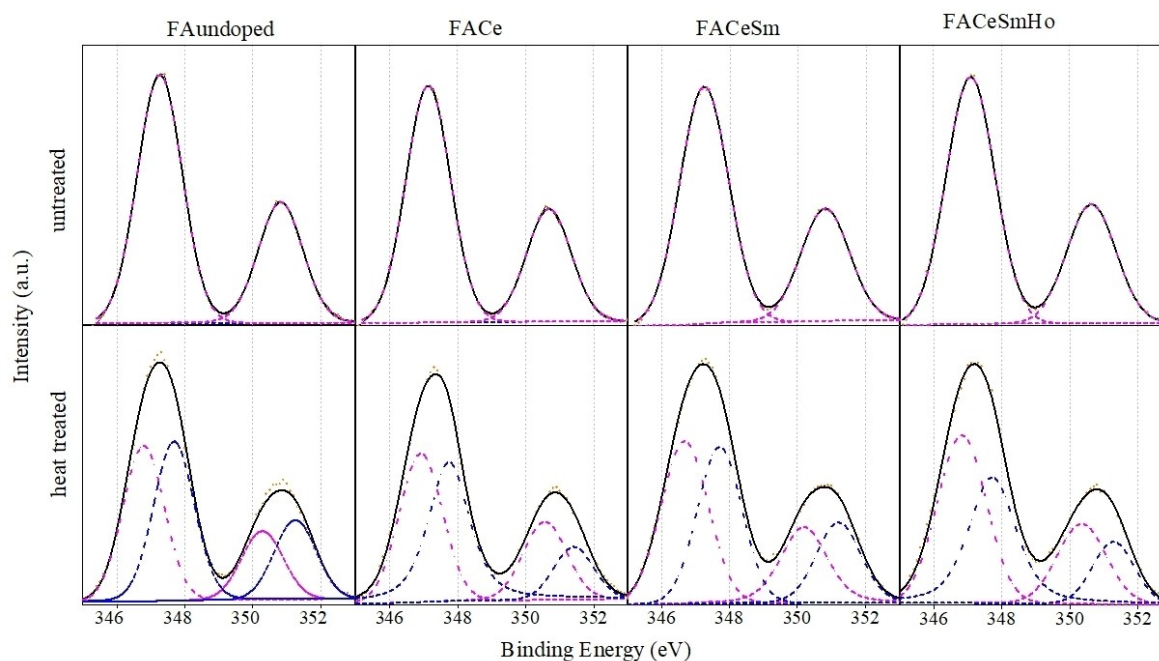


**Figure 11.** Comparison of High-resolution XPS spectra of Ca 2p of FA, FACe, FACeSm, and FACeSmHo before and after heat treatment.

environment of the P–O bonds within the apatite structure (supplementary Table ST4).

### 2.3. Determination of Oxidation States of Rare Earth Ions in the Apatite Lattice

The oxidation state and chemical environment of rare earth ions (cerium, samarium, and holmium) in the apatite structure were determined using high-resolution XPS spectra. Figure 12 shows the comparison of the high-resolution XPS spectra of cerium ions in the samples synthesized before and after heat treatment.

A quantitative assessment was conducted to discern changes in the cerium oxidation state. This involved performing curve-fitting on the X-ray photoelectron spectroscopy (XPS) spectra using multi-peak Gaussian/Lorentzian functions applied to the peak features. The deconvolution results of the cerium 3*d* XPS spectra of FA, FACe, FACeSm, and FACeSmHo before and after heat treatment are shown in Figure 12. There is evidence of the coexistence of the Ce<sup>3+</sup> and Ce<sup>4+</sup> states (as a Ce<sup>4+</sup>/Ce<sup>3+</sup> redox pair). Five doublets (v for Ce 3*d*<sub>5/2</sub> and u for Ce 3*d*<sub>3/2</sub>) were formed by deconvoluting the Ce 3*d* envelope. Ce<sup>3+</sup> species include v<sub>0</sub>, v, u<sub>0</sub>, and u; Ce<sup>4+</sup> species include v', v'', v''', u', u'', and u'''. Ce 3*d*<sub>5/2</sub> level peaks are located in the energy range between around 877 and 903 eV. Two peaks at 881–882 and 885–886 eV were assigned to the Ce<sup>3+</sup> state, whereas three peaks at 882–883, 889–890, and 898–899 eV were attributed to the Ce<sup>4+</sup> oxidation state.<sup>[27,30]</sup>

By determining the peak area of the u(0) v(0) and u(v) in relation to the area of the total Ce 3*d* region, the Ce<sup>3+</sup>/(Ce<sup>3+</sup> +

Ce<sup>4+</sup>) ratio present in the samples was calculated.<sup>[31–33]</sup> The dynamic interchange between Ce<sup>3+</sup> and Ce<sup>4+</sup> oxidation states is enabled by the generation of oxygen vacancies, allowing cerium ions to adapt their electronic configuration without structural modifications. Cerium ions readily fine-tune their electronic states to suit the surrounding conditions, manifesting oxygen vacancies or lattice defects through the loss of oxygen or its electrons. Ce<sup>4+</sup> with its low formation energies for surface vacancies plays a vital role in oxidation, while Ce<sup>3+</sup> and electron redistribution within lattice oxygen vacancies facilitate reduction processes. Importantly, the addition or removal of oxygen atoms during oxidation or reduction minimally disrupts the arrangement of cerium ions, ensuring the preservation of the apatite structure.<sup>[27]</sup> The calculated percentage of Ce<sup>3+</sup> and Ce<sup>4+</sup> of as-synthesized and after-heat treatment are shown in Table 6.

The uniqueness of samarium originates from the constant competition between its two stable valence states, Sm<sup>2+</sup> and Sm<sup>3+</sup>. In Figure 13, the Sm 3*d* envelope is displayed. The Sm 3*d*<sub>5/2,3/2</sub> peaks from 1085.2–1111.9 eV were attributed to Sm<sup>3+</sup>, with additional peaks between 1096–1121.5 eV for Sm<sup>2+</sup> 3*d*<sub>5/2,3/2</sub>.<sup>[34]</sup> The Sm 3*d* XPS spectra were analyzed and fitted into two doublets, with 'v' indicating Sm 3*d*<sub>5/2</sub> and 'u' indicating Sm 3*d*<sub>3/2</sub>. The values 'v<sub>0</sub>' and 'u<sub>0</sub>' are associated with Sm<sup>3+</sup> species, while 'v' and 'u' are associated with Sm<sup>2+</sup> species. The percentage of Sm<sup>3+</sup> and Sm<sup>2+</sup> was calculated similarly as was done for Ce<sup>3+</sup> in the previous section. The percentages of Sm<sup>3+</sup>/Sm<sup>2+</sup> peaks for both as-synthesized samples and after-heat treatment are displayed in Table 7. The electronic charges required for the formation of Sm<sup>3+</sup> and Sm<sup>2+</sup> ions in the apatite matrix are caused by oxygen-related vacancies. In addition to the effect of

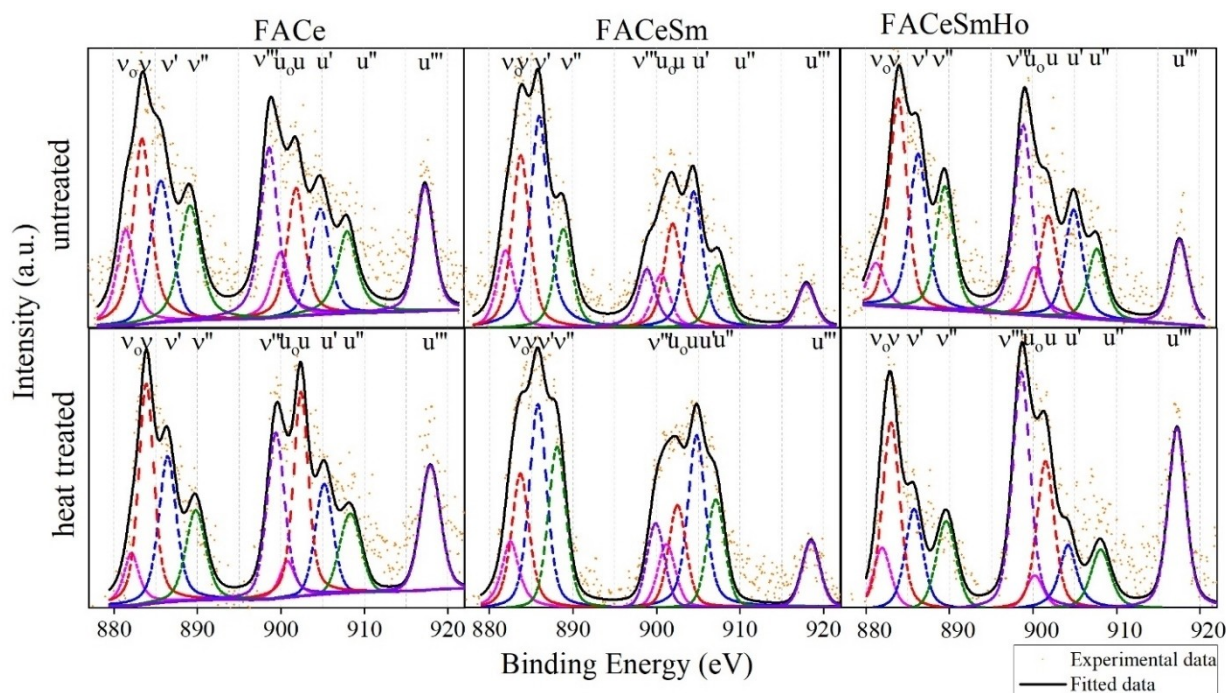


**Figure 12.** Comparison of High-resolution Ce 3*d* XPS spectra of FACe, FACeSm, and FACeSmHo before and after heat treatment. Cerium ions are present in Ce<sup>3+</sup> and Ce<sup>4+</sup> oxidation states.

Sample/sample condition	As synthesized	After heating
FACe	Ce <sup>3+</sup> = 33.4%; Ce <sup>4+</sup> = 66.5%	Ce <sup>3+</sup> = 30.1%; Ce <sup>4+</sup> = 70.9%
FACeSm	Ce <sup>3+</sup> = 47.7%; Ce <sup>4+</sup> = 52.2%	Ce <sup>3+</sup> = 45.3%; Ce <sup>4+</sup> = 54.6%
FA CeSmHo	Ce <sup>3+</sup> = 34.1%; Ce <sup>4+</sup> = 65.9%	Ce <sup>3+</sup> = 23.3%; Ce <sup>4+</sup> = 76.6%

charged defects/vacancies, it is probable that the chemical environment supplied by the oxygen species present in the apatite matrix itself favored the coexistence of Sm<sup>3+</sup>/Sm<sup>2+</sup> ions.<sup>[35,36]</sup>

The XPS analysis of Ho 3*d* spectra revealed its existence as Ho<sup>3+</sup> in the lattice before and after heat treatment. The spectrum of Ho 3*d*<sub>5/2,3/2</sub> with spin-orbit splitting  $\delta=40.1$  eV is observed at a weighted average binding energy of 1352.2 eV (supplementary Figure S10).<sup>[37,38]</sup>

### 3. CaP Phase Distinction Using X-Ray Photoelectron Spectroscopy Results

The samples formed after heat treatment were a mixture of stoichiometric apatites and tricalcium phosphates as observed from XRD results. Ca/P XPS ratios were used to identify the

Sample/sample condition	As synthesized	After heating
FACeSm	Sm <sup>3+</sup> = 80.2%; Sm <sup>2+</sup> = 19.8%	Sm <sup>3+</sup> = 68.7%; Sm <sup>2+</sup> = 31.3%
FACeSmHo	Sm <sup>3+</sup> = 69.4%; Sm <sup>2+</sup> = 30.6%	Sm <sup>3+</sup> = 60.8%; Sm <sup>2+</sup> = 39.1%

amount of stoichiometric apatite and tricalcium phosphate formed after heat treatment. Table 8 shows the calculated Ca/P atomic ratios, derived directly from the XPS data using atomic sensitivity factors. These ratios serve as a quantitative measure, enabling the determination of the proportions of tricalcium phosphate and stoichiometric apatite formed during the cooling process.<sup>[26]</sup>

The calculated Ca/P ratio of the heat-treated samples was each equated to a linear Equation (2)

$$R_i = xR_{TCP} + (1-x)R_{SFA} \quad (2)$$

where ' $R_i$ ' is the measured ratio for species ' $i$ ' (FA, FACe, FACeSm, FACeSmHo) after heat treatment. ' $x$ ' is the mole fraction of tricalcium phosphate formed and '(1- $x$ )' of the stoichiometric apatite present in the species ' $i$ '. Figure 14 shows the molar fractions of tricalcium phosphate and stoichiometric apatite generated in FA, FACe, FACeSm, and FACeSmHo. The amount of tricalcium phosphate produced after heat treatment for FA, FACe, FACeSm, and FACeSmHo was 34%, 32%, 25%, and 30%,

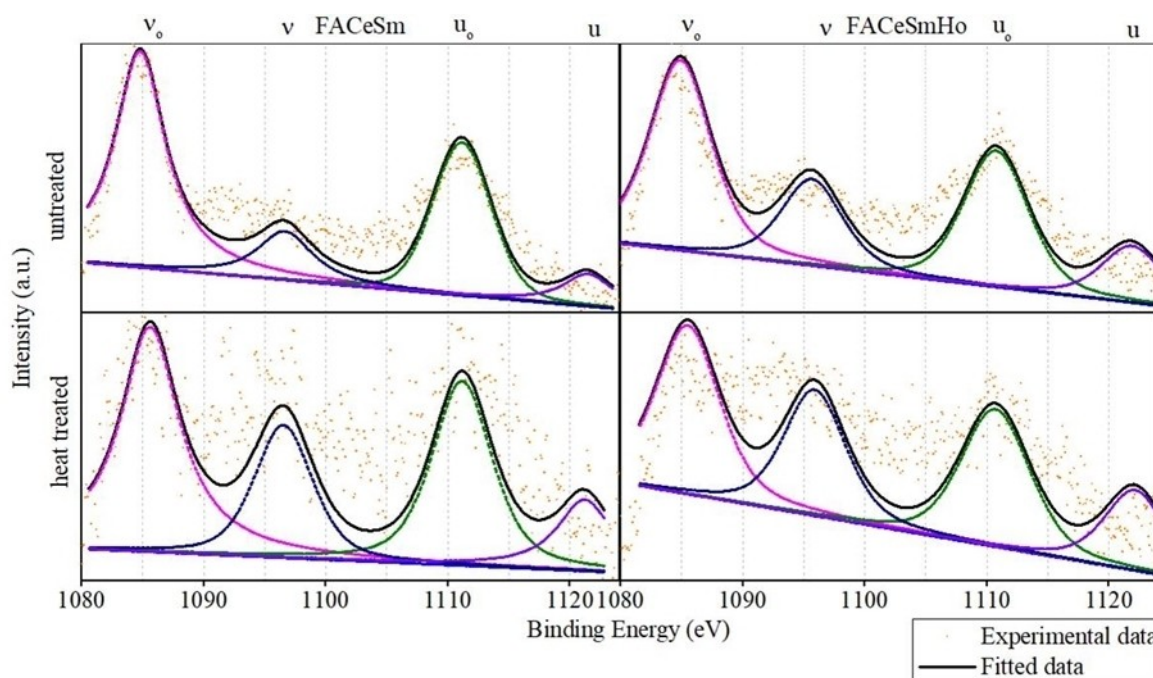


**Figure 13.** Comparison of High-resolution Sm 3*d* XPS spectra of FACeSm and FACeSmHo before and after heat treatment. Samarium is present in Sm<sup>3+</sup> and Sm<sup>2+</sup> oxidation states. The Sm<sup>2+</sup> ions have increased after heat treatment.

Table 8. The Ca/P atomic ratios calculated using XPS in the synthesized materials.			
Unheated	Ca/P ratio	Heat treated	Ca/P ratio
FA	1.66 ± 0.04	FA	1.60 ± 0.09
FACe	1.65 ± 0.02	FACe	1.59 ± 0.09
FACeSm	1.65 ± 0.02	FACeSm	1.62 ± 0.03
FACeSmHo	1.65 ± 0.02	FACeSmHo	1.61 ± 0.05

respectively. It is noteworthy that the inclusion of rare earth ions in the lattice resulted in a reduction in the percentage of tricalcium phosphate in the rare-earth-doped samples. This observation underscores the influence of rare earth doping on the phase composition of the synthesized materials, a crucial aspect in tailoring the properties of the apatite structure.

#### 4. Plausible Mechanism for the Formation of Tricalcium Phosphate

The XPS analysis revealed that holmium existed solely in the  $\text{Ho}^{3+}$  oxidation state within the apatite lattice, while cerium and samarium ions exhibited multiple oxidation states ( $\text{Ce}^{3+}$ ,  $\text{Ce}^{4+}$ ,  $\text{Sm}^{2+}$ ,  $\text{Sm}^{3+}$ ). The presence of multiple oxidation states within the lattice was attributed to the charge compensation principle. In the FACe lattice, approximately 36.5% of cerium was identified as  $\text{Ce}^{3+}$  and 66.5% as  $\text{Ce}^{4+}$ . The introduction of two  $\text{Ce}^{3+}$  oxidation states resulted in the creation of an oxygen vacancy within the apatite lattice for charge compensation. Similarly, one  $\text{Ce}^{4+}$  ion caused the formation of one oxygen ion vacancy. The concentration of  $\text{Ce}^{4+}$  ions correlated with an

increased number of vacancies in the lattice, resulting in more oxygen vacancies as the  $\text{Ce}^{4+}$  ion concentration rose.

Jun-Ming Liu conducted Monte Carlo simulations, discovering the critical role of vacancies in the phase separation of binary alloys.<sup>[39]</sup> As the temperature increased, more  $\text{Ce}^{3+}$  ions were converted to  $\text{Ce}^{4+}$ , leading to an increased number of vacancies. These vacancies played a role in regulating the kinetics of phase separation and influencing the local environment surrounding calcium ions. The self-aggregation and segregation of these vacancies onto two-phase boundaries eventually led to the formation of tricalcium phosphate.

In the case of FACeSm, the addition of samarium resulted in 47.7% of cerium ions existing as  $\text{Ce}^{3+}$  and 52.2% as  $\text{Ce}^{4+}$ , while  $\text{Sm}^{3+}$  and  $\text{Sm}^{2+}$  were present at percentages of 80.2% and 19.8%, respectively. Notably, the addition of samarium ions increased the  $\text{Ce}^{3+}$  ion concentration within the lattice. Upon heating, a slight increase in  $\text{Ce}^{4+}$  ion concentration ( $\text{Ce}^{3+} = 45.3\%$ ;  $\text{Ce}^{4+} = 54.6\%$ ) occurred, along with an increase in the  $\text{Sm}^{2+}$  ion concentration ( $\text{Sm}^{3+} = 68.7\%$ ;  $\text{Sm}^{2+} = 31.3\%$ ).  $\text{Sm}^{2+}$  ions did not lead to vacancy formation due to their charge equivalence with  $\text{Ca}^{2+}$ . The interplay between  $\text{Ce}^{3+}$  ion oxidation and  $\text{Sm}^{3+}$  ion reduction controlled the formation of vacancies. The reduced number of vacancies in FACeSm resulted in a lesser amount of tricalcium phosphate formation after heat treatment.

Furthermore, the ionic radii of the rare earth (RE) ions played a significant role in the stabilization and decomposition at high temperatures. The small size of the  $\text{Ho}^{3+}$  ion caused minimal lattice stress but led to the production of more vacancies than in FACeSm, ultimately increasing the production of tricalcium phosphate in FACeSmHo after heat treatment.

#### 5. Conclusions

Apatites containing rare earth ions (cerium, samarium, and holmium) were synthesized through a sol-gel process and rod-

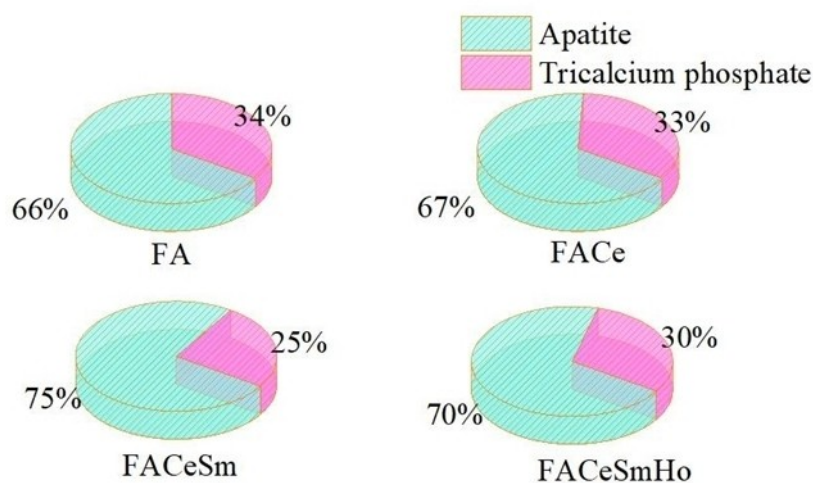


Figure 14. Amount of tricalcium phosphate and stoichiometric apatite formed after heat treatment. The FACeSm contains the least amount of tricalcium phosphate.

shaped particles were produced. The study revealed that adding rare earth ions to the apatite structure had a significant impact on the decomposition process and the creation of lattice vacancies. As a result, tri-calcium phosphate formation was affected, leading to varying levels of tri-calcium phosphate in different samples after cooling to room temperature. The FACeSm sample had the lowest percentage (25 %) of tri-calcium phosphate, while the FA, FACe, and FACeSmHo samples showed percentages of 34%, 32%, and 30%, respectively. The present study provides a comprehensive understanding of how apatite structures respond to high-temperature conditions in the presence of rare earth ions. The knowledge can significantly improve the utilization of apatite-based materials in various high-temperature processes such as calcination, sintering, hydrothermal processing, and plasma spraying. This study demonstrates the versatility and adaptability of apatite-based materials in industries where stability and high-temperature performance are crucial such as ceramic manufacturing, thermal barrier coatings, and high-temperature catalysts.

## Acknowledgements

The authors would like to acknowledge the European Union's Horizon 2020 Research and Innovation Programme under Grant Agreement No 953128 and UKRI Grant Ref: EP/X032612/1 for providing financial support. We further thank LEMAS and Bragg's Centre, University of Leeds for providing characterization facilities. Special thanks to Zabeada Aslam and Andrew Britton for helping in carrying out HRTEM and XPS experiments.

## Conflict of Interests

The authors declare no conflict of interest.

## Data Availability Statement

The data that support the findings of this study are available from the corresponding author upon reasonable request.

**Keywords:** Apatite · Phase decomposition · X-ray photoelectron spectroscopy · Rare earth ions

- [1] M. Pasero, A. R. Kampf, C. Ferraris, I. V. Pekov, J. Rakovan, T. J. White, *Eur. J. Mineral.* **2010**, *22*, 163–179.  
 [2] H. Shi, Z. Zhou, W. Li, Y. Fan, Z. Li, J. Wei, *Crystals (Basel)* **2021**, *11*, 1–18.  
 [3] T. G. P. Galindo, Y. Chai, M. Tagaya, *J Nanomater* **2019**, *2019*, 23.  
 [4] A. Ressler, A. Žužić, I. Ivanišević, N. Kamboj, H. Ivanković, *Open Ceramics* **2021**, *6*, 100122.

- [5] N. Leroy, E. Bres, D. B. Jones, S. Downes, *Eur. Cell. Mater.* **2001**, *2*, 36–48.  
 [6] J. Zeglinski, M. Nolan, M. Bredol, A. Schatte, S. A. M. Tofail, *PCCP* **2012**, *14*, 3435–3443.  
 [7] N. Leroy, E. Bres, D. B. Jones, S. Downes, *Eur. Cell. Mater.* **2001**, *2*, 36–48.  
 [8] E. N. Bulanov, K. S. Stasenko, O. N. Golitsyna, V. M. Kyashkin, A. V. Knyazev, *Ceram. Int.* **2022**, *48*, 9858–9863.  
 [9] A. D. Anastasiou, C. L. Thomson, S. A. Hussain, T. J. Edwards, S. Strafford, M. Malinowski, R. Mathieson, C. T. A. Brown, A. P. Brown, M. S. Duggal, A. Jha, *Mater. Des.* **2016**, *101*, 346–354.  
 [10] S. F. Ou, S. Y. Chiou, K. L. Ou, *Ceram. Int.* **2013**, *39*, 3809–3816.  
 [11] Y. Chen, X. Miao, *Biomaterials* **2005**, *26*, 1205–1210.  
 [12] A. Chaabouni, C. Chtara, H. Ben Abdallah, S. Taktak, A. Nzihou, H. El Feki, *International journal of scientific & technology research* **2017**, *6*, 8.  
 [13] S. F. Ou, S. Y. Chiou, K. L. Ou, *Ceram. Int.* **2013**, *39*, 3809–3816.  
 [14] N. V. Bulina, S. V. Makarova, S. G. Baev, A. A. Matvienko, K. B. Gerasimov, O. A. Logutenko, V. S. Bystrov, *Minerals* **2021**, *11*, 1310.  
 [15] N. G. Chernorukov, A. V. Knyazev, E. N. Bulanov, *Inorg. Mater.* **2011**, *47*, 172–177.  
 [16] K. Tõnsuaadu, K. A. Gross, L. Pluduma, M. Veiderma, in *J. Therm. Anal. Calorim* **2012**, 647–659.  
 [17] A. D. Anastasiou, M. Nerantzaki, E. Gounari, M. S. Duggal, P. V. Giannoudis, A. Jha, D. Bikiaris, *Sci. Rep.* **2019**, *9*, 14469.  
 [18] M. E. Fleet, *Am. Mineral* **1997**, *82*, 870–877.  
 [19] J. M. Hucnrs, M. Cevrno, *Am. Mineral* **1989**, *74*, 870–876.  
 [20] M. E. Fleet, Y. Pan, *Am. Mineral* **1995**, *80*, 329–335.  
 [21] J. Terra, E. R. Dourado, J. G. Eon, D. E. Ellis, G. Gonzalez, A. M. Rossi, *PCCP* **2009**, *11*, 568–577.  
 [22] A. V. Knyazev, N. G. Chernorukov, E. N. Bulanov, *Mater. Chem. Phys.* **2012**, *132*, 773–781.  
 [23] A. V. Knyazev, E. N. Bulanov, V. Z. Korokin, *Mater. Res. Bull.* **2015**, *61*, 47–53.  
 [24] B. O. Fowler, *Inorg. Chem.* **1974**, *13*(1), 194–207.  
 [25] F. Bakan, O. Laçin, H. Sarac, *Powder Technol.* **2013**, *233*, 295–302.  
 [26] H. B. Lu, C. T. Campbell, D. J. Graham, B. D. Ratner, *Anal. Chem.* **2000**, *72*, 2886–2894.  
 [27] P. Phatai, C. M. Futralan, S. Utara, P. Khemthong, S. Kamonwannasit, *Results Phys.* **2018**, *10*, 956–963.  
 [28] B. Demri, D. Muster, *J. Mater. Process. Technol.* **1995**, *55*, 311–314.  
 [29] G. C. Gomes, F. F. Borghi, R. O. Ospina, E. O. López, F. O. Borges, A. Mello, *Surf Coat Technol.* **2017**, *329*, 174–183.  
 [30] L. Truffault, M. T. Ta, T. Devers, K. Konstantinov, V. Harel, C. Simmonard, C. Andrezza, I. P. Nevirkovets, A. Pineau, O. Veron, J. P. Blondeau, *Mater. Res. Bull.* **2010**, *45*, 527–535.  
 [31] U. Berwal, V. Singh, R. Sharma, *J. Lumin* **2023**, *257*, 119687.  
 [32] R. Génois, S. Jobic, G. Ouvrard, F. Massuyeau, R. Gautier, *Appl. Mater. Today* **2020**, *20*, 100643.  
 [33] Y. Wu, F. Meng, Q. Li, M. Koschan, C. L. Melcher, *Phys. Rev. Appl.* **2014**, *2*, 044009.  
 [34] A. R. Zanatta, *Opt. Mater Express* **2016**, *6*, 2108.  
 [35] A. R. Zanatta, *J. Appl. Phys.* **2012**, *111*, DOI: 10.1063/1.4729911.  
 [36] A. R. Zanatta, C. T. M. Ribeiro, U. Jahn, *Appl. Phys. Lett.* **2001**, *79*, 488–490.  
 [37] B. Sriram, J. N. Baby, Y. F. Hsu, S. F. Wang, M. George, *Inorg. Chem.* **2021**, *60*, 12425–12435.  
 [38] K. I. Maslakov, Y. A. Teterin, O. I. Stefanovskaya, S. N. Kalmykov, A. Y. Teterin, K. E. Ivanov, S. S. Danilov, S. V. Yudin, B. F. Myasoedov, *Radiochemistry* **2021**, *63*, 801–810.  
 [39] J.-M. Liu, *Scr. Mater.* **1997**, *37*, 535–541.

Manuscript received: January 31, 2024  
 Revised manuscript received: May 12, 2024  
 Accepted manuscript online: June 18, 2024  
 Version of record online: August 22, 2024